

# Transport mechanism in a photoelastic chute flow in view of the evolution of force networks

Fu-Ling Yang,<sup>1,\*</sup>, Guan-Rui Chen<sup>1</sup>, and Cheng-Cheng Chu<sup>1</sup>

<sup>1</sup>Mechanical Engineering, National Taiwan University, 10617 Taipei, Taiwan

**Abstract.** This work adopts high-speed imaging analysis to measure the flow dynamics and the force chain properties for steady chute flows of photoelastic circular disks with fast-changing fringe patterns. We adopt the granular kinetic theory to evaluate collision-based stress components while calibrating the fringe-based force chain properties to evaluate the friction-based stress components. The fringe images allow us to define a new penetration band to clarify the spatial extent of pure-collisional and pure-frictional transport and a possible transition in the mid-layer, within which grain rotation is promoted, which may be associated with the breaking of the force network. Superposition of the collision- and the friction-based stress evaluation does not recover the hydrostatic depth profiles, highlighting an unaddressed transport mechanism or deficiency in the measurement technique.

## 1 Background

A granular flow can be multi-phasic as the constituent grains may undergo repulsive collisions or lasting frictional contacts to transport unbalanced momentum flux. Several constitutive models have been proposed, including the granular kinetic theory, the fluidity-based model, and the local  $\mu(I)$  rheology model. In the latter,  $\mu = \tau/p$  is the effective friction coefficient depending on the ratio of bulk tangential ( $\tau$ ) to its mean normal stress ( $p$ ), and  $I$  is the inertial number that characterizes the grain mobility tendency along and transverse to a flow. While most of these models find success in capturing flow phenomena that rely on collision-based transport, insufficiency appears when a flow transits towards a less fluidized state, where grains alternate between the collisional and frictional interactions. The constituent grains can even form long-lasting frictional contact with multiple neighbours that form force chain networks across the flow, providing an alternative transport mechanism other than collision-based diffusion.

Aranson *et. al* [1] performed discrete element simulations to study how such a mode transition of particle interactions affects bulk rheological behaviors. They scrutinize the mean interaction force of each grain to see if it exceeds or falls below a threshold to label if the interaction force contributes to a friction-based or collision-induced stress counterpart. Via such mode bisection, they show how the frictional component  $\mu_f$  decreases monotonically with  $I$  while the collisional counterpart  $\mu_c$  grows and asymptotes to a constant at large  $I$ , resuming the classical  $\mu(I)$  relation.

However, most of the existing studies on how the force network affects bulk rheological behavior rely on

particle-based simulation. Experimental investigation is scanty, and there is yet no experimental evidence directly showing the conversion of collision-induced stress into the friction counterpart. Hence, this work follows the classical work [2] to exploit the birefringence property of photoelastic disks and high-speed imaging analysis to attempt non-intrusive and concurrent measurement of flow dynamics and its stress components for a steady inclined surface flow. To promote the friction-induced stress, flow conditions were chosen carefully near the material's arrest state.

## 2 Experimental setup and data analysis

We have developed a chute facility to generate steady flows of photoelastic circular disks at a specific inclination angle  $\theta$  as sketched in Fig.1(a). The chute has a large upstream reservoir connected to a downstream flow area that is 150 cm in length, 20 cm in height, and has a uniform 0.35 cm narrow gap between two identical glass side walls. The experimental disks were manually cut from a Vishay PS-4 photoelastic sheet of 3mm thickness in 5mm- and 7mm-diameter, and an equal number of each size was mixed before filling into the upstream reservoir. By controlling the chute inclination angle and the reservoir gate height  $H_g$ , we can create steady flows of photoelastic granular disks of different mass flow rates. An acrylic bar with evenly gapped semi-circular bumps (6mm in diameter and spacing) was fixed to the chute base to ensure a no-slip boundary within the examined flow conditions, as shown in Fig.1b. The  $h_{\text{stop}}-\theta_{\text{stop}}$  and  $h_{\text{start}}-\theta_{\text{start}}$  relations for the granular mixture were measured on the chute as shown in Fig. 2(b), based on which four test conditions were set by

\* Corresponding author: [fulingyang@ntu.edu.tw](mailto:fulingyang@ntu.edu.tw)

choosing the gate height and the chute inclination angle above the  $h_{\text{start}}-\theta_{\text{start}}$  curve as marked.

A high-speed digital camera (PCO.dimax HS with NIKON 2184 AF-S NIKKOR 24 mm f1.4-f16 lens) was set 20 cm upstream of the exit to record the flow dynamics at the frame rate of 500 per second (FPS) with an exposure time of 1000-2000 $\mu$ s. A large LED light panel (FOTGA, LED1120, 13800 LM) was set with a homogenizer and a monochromatic filter to provide illumination from the other side of the chute. A pair of circular polarizers was placed on both sides of the chute to pass only the light through loaded disks exploiting the birefringence property of the photoelastic disks.

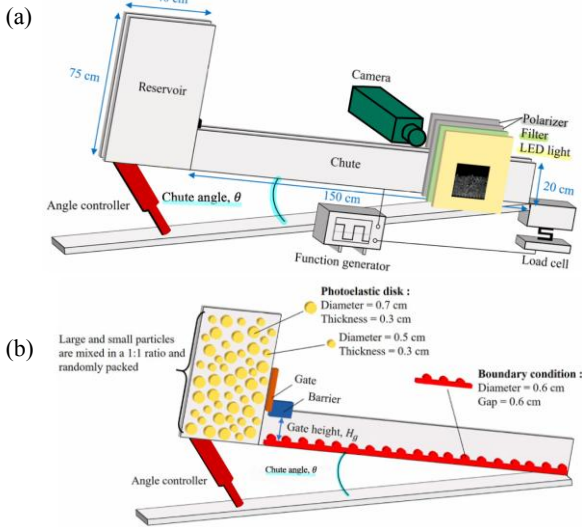


**Fig. 1.** Schematic diagram of the photoelastic granular flow chute: (a) the overall layout, (b) the test materials and the prepared basal condition [4].

Flow steadiness was monitored by measuring the accumulated discharge mass in time,  $m(t)$ , at the exit of the chute via a load cell that is synchronized with the high-speed digital camera and recorded via an NI DAQ system. The normalized accumulated mass flow rate,  $m^*$ , shown in Fig.2(b) is examined to determine over which duration the recorded images should be analyzed (when  $m^*$  fell between the chosen upper and lower bounds marked on the plot). A typical experimental image is shown in Fig.3(a) where both the disks and the photoelastic fringes were visible. A steady flow height,  $H_f$ , can be determined via binarizing the grayscale images. The resulting  $(H_f, \theta)$  are also marked on Fig.2(a) to ensure they fall above the mean  $h_{\text{start}}-\theta_{\text{start}}$  curve.

In-house image processing MATLAB routines have been developed to locate photoelastic disks with and without photoelastic fringes as shown in Fig.4(a). The method of the nearest neighbour was further applied to achieve Particle tracking velocimetry (PTV) and the instantaneous grain velocity vectors,  $\underline{u}_{pi}(t)$ , are illustrated by the white arrows therein. A spatial averaging rectangle that spans 20D in length and 3D in height was used to compute an instantaneous bulk property, which is averaged over 1000 images to estimate a mean value. By shifting the averaged box by 1D from the flow base to the free surface, we obtained the depth profiles of bulk solid volume fraction  $\phi(y)$ ,

streamwise velocity,  $u(y)$ , and granular temperature,  $T(y)$ , as shown in Fig.4(a)-(c), respectively.

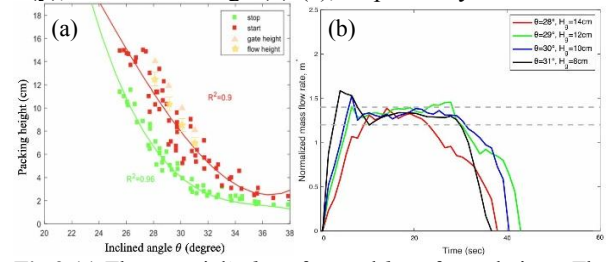


**Fig.2** (a) The material's  $h_{\text{stop}}-\theta_{\text{stop}}$  and  $h_{\text{start}}-\theta_{\text{start}}$  relations. The chosen test conditions ( $\blacktriangle$ ) and the resulting flow states ( $\star$ ) are all above the mean flow onset curve, (b) Normalized mass flow rate under the four flow conditions. Only the flow dynamics with  $m^*(t)$  falling in the marked range was analyzed.

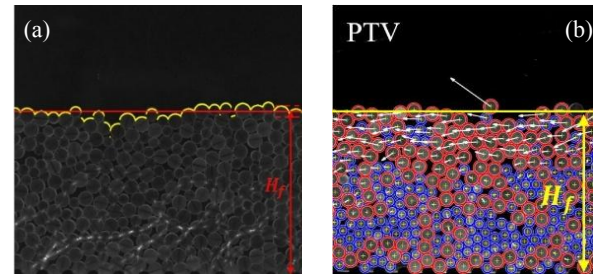


**Fig.3** (a) Snapshot of one experimental image. The free surface was captured to evaluate an instantaneous flow height,  $H_f$ ; (b) the results of instantaneous particle locating and particle tracking velocimetry (PTV).

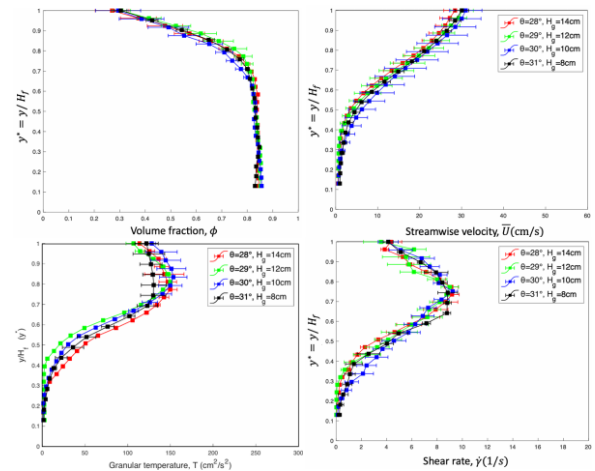


**Fig.4** Depth profiles of mean solid volume fraction  $\phi$ , streamwise velocity  $\bar{U}$ , granular temperature,  $T$ , and bulk shear strain rate,  $\dot{\gamma}$ .

Next, we assume that frictional contacts occur on grains exhibiting light fringes, as these fringes become visible only when the grain is subject to a mean compression force above some threshold. Such a physical threshold is conceptually equivalent to how the particles are separated into frictional and collisional contacts in [1]. As expected, most of the fringes were observed in the deeper layer near the chute base (see Fig. 3(a)) for the greater confining pressure. We developed a second MATLAB routine to extract the bright patches at the end of the fringes within each disk, near the contact points. The patch centroid was determined and joined by line segments whose slopes were adopted to evaluate a fringe angle  $\alpha_i$  relative to the chute base. This is done for each particle in a force network, as sketched in the inset of Fig.5(a). The arithmetic intensity of each particle's contact patches is evaluated,  $\bar{I}_i$ , together with

the total patch area within each disk,  $A_i$ , to perform a weighted average within the average box,  $\alpha(t) = \sum_i A_i \bar{I}_i \alpha_i / \sum_i A_i \bar{I}_i$ , before taking the temporal average into  $\langle \alpha \rangle$ . The classical  $G2(t)$  value that sums over the square of the intensity gradient of each grain pixel in the same average box as also computed at one moment by the expression shown next to Fig.5(a). In the expression,  $I_{i,j}$  denotes the light intensity at the  $(i, j)$  pixle and  $N$  is the number of disks falling in the average box. This instantaneous value was averaged in time into  $\langle G2 \rangle$ . The depth profiles of both quantities under the four flow conditions are shown in Fig.5(b) and 5(c), respectively.

Threading up these patch-joining segments can form a force network, as demonstrated by the network in blue. A new length scale—the fringe penetration length  $H_p$ —is proposed by the maximum height of the fringe patch. This length scale characterizes to what spatial extent a frictional contact force network can develop from the no-slip base so that the basal arresting impulse may propagate via a friction-based transport mechanism. As force chains break and rebuild during a flow, we monitor its ratio to the instantaneous flow height,  $H_p(t)/H_t(t)$  in Fig.6(a) to evaluate a temporal mean  $\{H_p/H_t\}$  and a standard deviation. A penetration band is proposed by the mean plus/ minus one deviation, which drops monotonically with the mean Froude number  $\{Fr\}$  in Fig.6(b), suggesting the diminishing role of friction-based transport in faster flows. Here, an

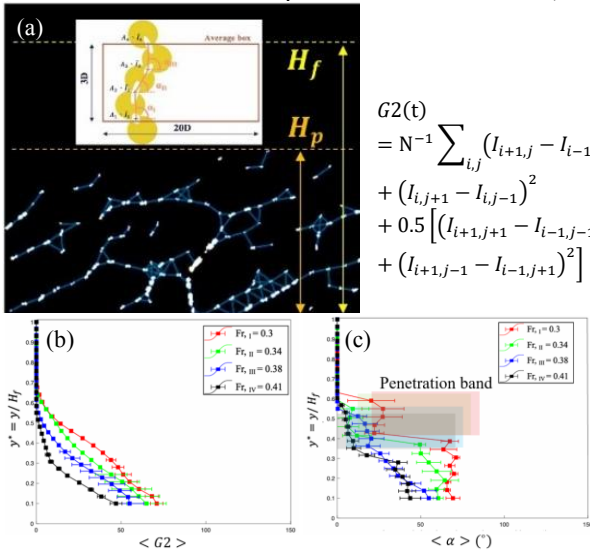


**Fig. 5** (a) The extracted fringe patches and the instantaneous contact network with individual fringe angles marked in the inset; the temporally and spatially averaged depth profiles for the fringe-based  $G2$  value and (c) the mean fringe angle.

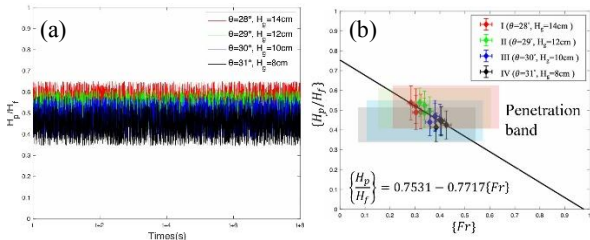


**Fig. 6** (a) Instantaneous fringe penetration height scaled by the instantaneous flow height  $H_t$ , (b) the temporal mean of  $H_p/H_t$  as a linearly decayed function of mean flow Froude number, evaluated by the surface velocity, flow height, and a depth-averaged volume fraction.

instantaneous Froude number was first calculated by the surface velocity and height at the same moment as  $Fr(t) = U_s(t) / [g \cos \theta H_t(t)]^{1/2}$  and then averaged over the observation period for  $\{Fr\}$ .

Interestingly, we mark the penetration bands under each  $\{Fr\}$  by colored blocks in Fig.6(b). When we overlaid this penetration band on the plot of  $\langle \alpha \rangle (y^*)$  in Fig.5(c), it is clear that  $\langle \alpha \rangle$  starts to grow from the upper band edge but seems to saturates to a plateau after the lower edge in the slowest flow (in red), while  $\langle \alpha \rangle$  in the other cases continue to grow towards the basal maximum value.

Other than photoelastic fringes, careful observation discovered the break of a force network always induces a sudden rotation of the released grains, suggesting it is the unbalanced torque that breaks the local frictional structure. Hence, special efforts were made to measure the disk angular velocity by tracing the lines manually marked on each disk before the experiment, as shown in Fig.7. These lines remained visible in the photoelastic images and can be extracted by a third MATLAB routine to evaluate their inclination angles [5].

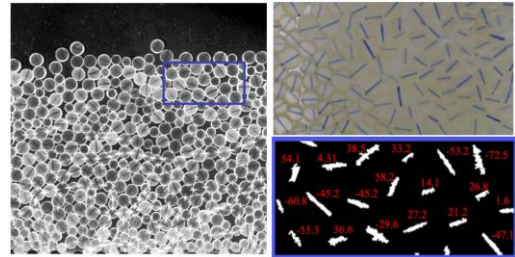


**Fig. 7** Photoelastic disks with newly added line marker (top right) with the extracted sloped angles (base right).

The change of this marker angle between two consecutive images was evaluated to estimate individual grain angular speed,  $\omega_i(t)$ . Spatial average with the same average box was performed followed by a temporal mean to obtain the depth profile of bulk angular speed  $\langle \omega \rangle (y^*)$  in Fig.8(a). In fact, we speculate the magnitude of the rotation-induced velocity at the contact point,  $R\omega_i(t)$  with  $R$  being the grain radius, relative to the translational speed,  $|\underline{u}_{pi}(t)|$ , to be an important parameter that characterizes the breaking tendency of a contact network. Hence, we further evaluate an individual instantaneous rotation index,

$$\Omega_i(t) = R\omega_i(t) / |\underline{u}_{pi}(t)|, \quad (1)$$

to examine the bulk rheology. The averaged depth profile of  $\langle \Omega \rangle (y^*)$  in Fig.8(b) grows within the penetration band and seems to peak beneath the lower edge of the band, except for the fastest case (in black).

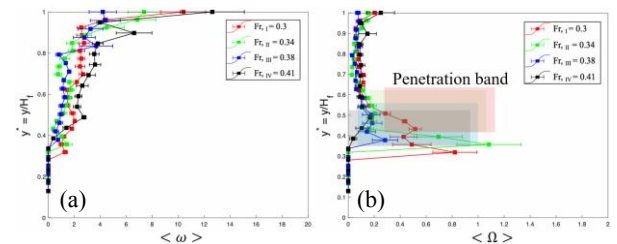


**Fig. 8** Depth profile of (a) particle angular speed, (b) the rotation index with the penetration band defined in Fig.5(b).

### 3 Bulk stress and discussion

To evaluate the collision-based stress, the measured flow variables in Fig.4 were inserted into the granular kinetic theory to evaluate the normal and tangential stress components across the flow layer according to [3]

$$\sigma_c = \rho \phi T (1 + 4\eta \phi g_0) \quad (2)$$

$$\tau_c = \frac{8}{3} \dot{\gamma} \left\{ \frac{2\mu_a}{\eta(2-\eta)g_0} \left( 1 + \frac{8}{5}\eta\phi g_0 \right) \left[ 1 + \frac{8}{5}\eta(3\eta-2)\phi g_0 \right] + \frac{6}{5}\mu_b\eta \right\} \quad (3)$$

$$g_0(\phi) = \frac{1}{2(1-\phi)} + \frac{1}{2(1-\phi)^2} + \frac{\phi}{16(1-\phi)^2} \quad (4)$$

where  $\mu_a = 5m\sqrt{T}/\pi / 16d^2$ ,  $\mu_b = 256\mu_a\phi^2 g_0 / 5\pi$ , and  $g_0(\phi)$  is the radial distribution function. The dissipation parameter,  $\eta = (1 + e_p) / 2$ , depends on the coefficient of restitution  $e_p$  between two photoelastic discs of mean mass and diameter  $m$  and  $d$ . Special efforts were made to hang the photoelastic discs as two pendulums to allow head-on collisions at their rims so that the coefficient of restitution needed in the theory can be measured to be  $e_p=0.41$  [4].

To calibrate the fringe properties for the normal and the tangential stress components, we captured images of static packing of different heights and  $\theta_s$ . We evaluated the  $G2$  value at a specific height and calibrated it with the corresponding normalized hydrostatic normal pressure,  $\rho_s\phi(y^*)g\cos\theta(1-y^*)$  with  $y^*=y/H_f$ , to fit  $\{\sigma_f^*\} = -0.49\{G2^*\}^2 + 1.3\{G2^*\} + 0.1$  for the normal frictional stress component. Here,  $\rho_s=1.139$  g/cm<sup>3</sup> is the material density, and the effect of packing heights and  $\theta_s$  are normalized by scaling out the maximums into  $G2^*$ . As for the tangential stress component, we observed the experimental images and found variations in the force chain morphology when the flow condition was changed. Hence, we propose to calibrate the static tangential stress with the mean fringe angle as  $\{\tau_f\} = 3.238 < \alpha > + 45.74$ , as a new strategy to evaluate friction-based tangential stress,  $\tau_f$ . We then analyzed the images during a flow to estimate a time-averaged depth profile for  $\sigma_f(y)$  and  $\tau_f(y)$ .

Finally, Fig.9(a) shows the results of the normal collisional and frictional stress profiles,  $\sigma_c(y^*)$  and  $\sigma_f(y^*)$ , for the two slower flows (due to page limit) and they are superposed  $\sigma(y^*)=\sigma_c(y^*)+\sigma_f(y^*)$  and compared to the hydrostatic profile solved from the steady fully-developed momentum equation. Likewise,  $\tau_c(y^*)$ ,  $\tau_f(y^*)$ , and their superposition,  $\tau(y^*)=\tau_c(y^*)+\tau_f(y^*)$ , are compared to the hydrostatic profiles in Fig.9(b). The corresponding penetration bands are also marked to visualize the spatial extent of the friction-based mechanism.

Interestingly, the total normal stress can be well captured by the granular kinetic theory above the penetration band and the  $G2$ -based fringe information, supporting that the stress is pure collisional and frictional in the surface and the basal layers, respectively. A transition does occur in the mid-layer around the penetration band for which the superposed value underestimates the true stress. Likewise, the granular kinetic theory provides a feasible description above the penetration band, except at the lowest  $\{Fr\}$ . A transition

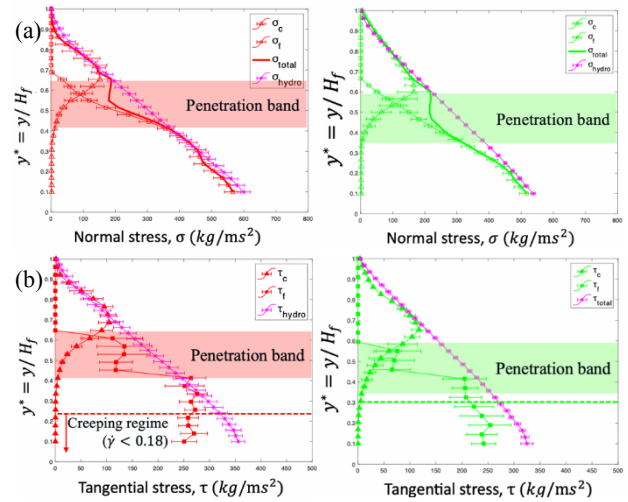


**Fig.9** Comparison of the theory-based collisional stress, the fringe-based frictional stress, their superposition, and the analytic hydrostatic depth profiles, for the (a) normal and (b) tangential stress components for two slower flow conditions.

to the frictional component is also found across the penetration band, but now the  $\alpha$ -based evaluation severely underestimates the frictional tangential stress in the deeper bed though  $\tau_f(y)$  seems to grow with the immersion depth like the hydrostatic profile. Further investigation is required to clarify the discrepancy. Nonetheless, we hope to bring attention to the underestimation of  $\sigma(y^*)=\sigma_c(y^*)+\sigma_f(y^*)$  in the penetration band, which may be associated with the promoted degree of rotation-induced sliding velocity at the contacts relative to its translation upon chain breaking. The onset of rotation may cause extra momentum flux not addressed in both aspects, which motivates future research in this regard, possibly with extension to the classical Cosserat or micropolar theories. In addition, it is noted that different  $g_0(\phi)$  have also been tested but Eq.(4) provides the best fit of  $\sigma_c(y^*)$  to the hydrostatic profile in the surface layer, even when the measured  $e_p=0.41$  may fall out of the scope of the granular kinetic theory. The success seems robust, which warrants further research with this pseudo-two-dimensional flow setup. It shall also be interesting to seek comparison with the theoretical prediction by the kinetic theory.

The authors acknowledge the research grants from the National Science and Technology Council, Taiwan via 112-2221-E-002 -137 -MY3 and 113-2923-E-002 -009.

#### Reference

1. I.S. Aranson, L.S. Tsimring, F. Malloggi, Phys. Rev. E. **78**, 031303 (2008)
2. D. Howell, R.P. Behringer, Phys. Rev. Lett. **82**, 26-28 (1999)
3. P.C. Johnson, P. Nott, R. Jackson, J. Fluid Mech. **210**, 501– 535 (1990)
4. G.R. Chen, Master Thesis, Mechanical Engineering, National Taiwan University, Taiwan, 2022
5. C.C. Chu, Master Thesis, Mechanical Engineering, National Taiwan University, Taiwan, 2023